Diathermy replica and Shadowgraph experiment

M. Augustin, , D. Harantová, J. Malina, J. Míchal, J. Rak[1]

[1]ELLIA foundation

January 26, 2026

Contents

1 Introduction **3**

2 Diathermy replica **4**
- 2.1 H-V transformer 5
- 2.2 Spark Gap Unit 7
- 2.3 Tesla Transformer used in DU 8
- 2.4 Coupling of Strongly Detuned Resonators 11
- 2.5 Damping of the Secondary Parallel Resonance 12
  - 2.5.1 Effective Inductive Loading and Secondary Modes 13
  - 2.5.2 Implications for Tesla Transformer Operation 13
  - 2.5.3 Minimal Impedance-Matrix Model for Two Magnetically Coupled Resonators 14
  - 2.5.4 Connection to the VNWA-Measured Frequency Response 15
- 2.6 Primary characteristic impedance 16

3 Tertiary Coil **17**
- 3.1 Problem statement: why the parallel peak collapses when the tertiary is attached 18
- 3.2 Equivalent-circuit interpretation (lumped + distributed) 19
- 3.3 Design objectives (Tesla-correct extra coil) 20
- 3.4 Concrete problems identified from the two plots 20
- 3.5 Mitigation strategy (VNA-driven, step-by-step) 21
  - 3.5.1 Step 1: Push the tertiary *series* resonance away from f_p 21
  - 3.5.2 Step 2: Keep the tertiary *parallel* resonance safely above the operating band 21
  - 3.5.3 Step 3: Tune with terminal capacitance, not with turns 21

3.5.4 Step 4: Minimize C_{jg} by physical placement and routing 22
3.5.5 Step 5: VNWA validation criteria 22
3.6 Summary: what is wrong and what fixes it 22

4 Desmitron tubes Optical and thermal spectra 24

5 Shadowgraph results 27

A Meaning and Role of a High-Q Resonant System 28

B Two coupled LC resonators 29
B.1 Eigenfrequencies 30
B.2 Eigenvectors and amplitude ratios 30
B.3 Hybridization versus localization 31
B.4 In-phase and out-of-phase normal modes 31

C Hybridized modes in a Tesla transformer: transference and displacement regimes 32
C.1 In-phase and out-of-phase hybridized modes 32
C.2 Transference and displacement in Maxwellian terms 33

D Quarter-wave condition of the tertiary (transmission-line) resonator 33

1 Introduction

At the end of the nineteenth century, Nikola Tesla pioneered the use of high-vacuum, high-frequency, single-electrode lamps capable of producing distinctive images known as *Shadowgraphs*. These images were generated by a form of penetrating radiation exhibiting transmission properties through matter comparable to X-rays, yet characterized by fundamentally different physical behavior. Tesla's work demonstrated that such radiation could be produced without conventional cathode–anode configurations, relying instead on impulsive, high-frequency excitation.

Inspired by this early research, G.G. Brock Laboratories developed and patented the *1A21 Desmitron* vacuum tube, representing a refined implementation of the Shadowgraph emitter concept. The device comprises a single light-element cathode enclosed within a glass envelope evacuated to approximately 10^{-7} Torr, mounted on a dielectric base. It is powered by high-frequency alternating current sources, such as Tesla coils or Oudin coils, and operates through disruptive discharge impulses rather than continuous direct current, thereby distinguishing it from conventional X-ray or electron-beam devices.

In July 2025, the ELLIA Laboratory entered into a collaborative partnership with G.G. Brock Laboratories, represented by Griffin Brock, and with QuantumHeat C.I.C., the organization operating the Martin Fleischmann Memorial Project, represented by Robert Greenyer and Paul Harris. The primary objective of this collaboration is to enable the replication of the 1A21 Desmitron tube within the European Union and to further develop and assess its potential scientific and technological applications.

A Memorandum of Understanding (MoU) formalizing this collaboration was signed in July 2025, thereby initiating the project. In September 2025, the construction and engineering of the first complete experimental system were carried out at the ELLIA Laboratory. Initial experimental results were obtained in November 2025; however, the intensity of the emitted radiation remains insufficient for the intended applications.

This document provides a detailed overview of the Desmitron project as conducted at the ELLIA Laboratory, including its historical context, system architecture, experimental implementation, and current challenges.

2 Diathermy replica

In September 2025, two *1A21 Desmitron* tubes were received from G.G. Brock Laboratories. In order to replicate the results previously reported by Griffin Brock, our initial objective was to construct a replica of the 1920s H. G. Fischer Diathermy Unit (DU) [1], which had been used by Griffin to power the Desmitron tube. The original schematic of the Fischer DU is shown in Fig. Fig. 1(a).

Subsequently, it was determined that Adrian Marsh had already completed a detailed replication of the Fischer Diathermy Unit and documented the process and design in [2]. As a result, we adopted his methodology and construction approach. The electrical schematic from [2] that was followed in the present work is shown in Fig. Fig. 1(b).

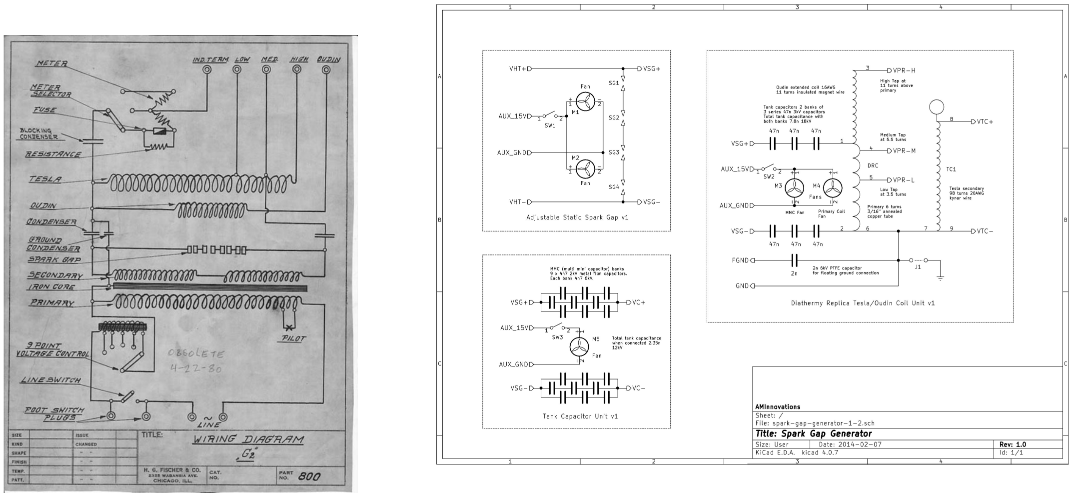

(a)

(b)

Figure 1: (a) Fisher Medical Diathermy [1]. (b) Spark gap generator schematic showing the static spark gap, the diathermy replica unit, and the tank capacitor unit taken from [2].

The current configuration of the Diathermy Unit (DU), supplemented with a tertiary coil and used for the Desmitron tube tests, is shown in Fig. 2. The high voltage is supplied by a transformer rated at 230 V/V_{RMS} = 7 kV, with the primary winding voltage regulated by a variac (for further details, see Section 2.1). The high-voltage output is subsequently connected to the spark gap unit (see Section 2.2) and to the primary winding of the Tesla transformer (see Section 2.3).

The primary resonant *LC* circuit consists of four 35 nF/30 kV capacitors connected in series, resulting in an effective primary capacitance of $C_{\mathrm{prim}} = 8.8$ nF. Each capacitor is shunted by a 10 MΩ/3 W resistor to equalize the voltage distribution across the capacitor stack. Without this protective measure, the first capacitor in the series chain was frequently damaged within a few milliseconds after spark-gap ignition.

In addition to the primary coil, an auxiliary coil with 11 turns, referred to as the Oudin coil, is incorporated into the system. The parameters of all coils used in the setup are summarized in Table 1. The secondary coil of the Tesla transformer is subsequently coupled to the tertiary coil (see Section 3) and to the Desmitron tube.

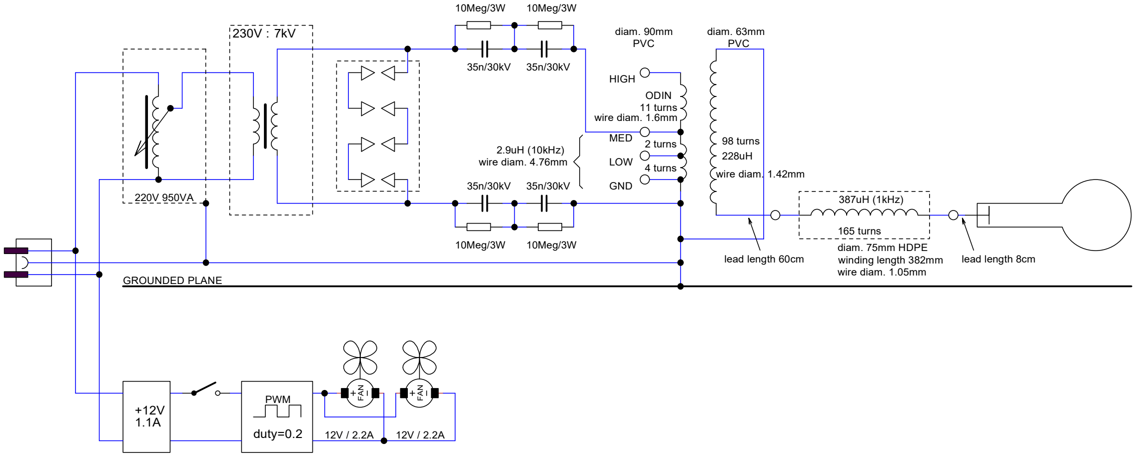

Figure 2: The DU configuration employed in this study. The high voltage is supplied by a $230V/V_{\text{RMS}} = 7$ kV, 7 kW transformer, with the primary winding voltage regulated by an autotransformer (see Section 2.1). The high-voltage output is then connected to the spark gap unit (see Section 2.2) and to the primary winding of the Tesla transformer (see Section 2.3). The secondary coil of the Tesla transformer is subsequently connected to the tertiary coil (see Section 3) and to the Desmitron tube.

2.1 H-V transformer

In the initial version of the Diathermy Unit, a microwave oven transformer (MOT) was used to supply the high voltage. Four MOTs were connected in a series–parallel configuration; however, this arrangement did not deliver sufficient power to the DU. Consequently, a custom-built high-voltage transformer was employed, with which the first positive signals were obtained.

The transformer was characterized by means of a short-circuit test to determine its current–voltage characteristics under load conditions. During the test, the transformer secondary was short-circuited, and the primary current was measured using a clamp ammeter, while the primary voltage was gradually adjusted by an autotransformer.

The following observations were made during characterization of the high-voltage transformer:

- No significant magnetic core saturation was observed over the full range of primary voltages (0–230 $\mathrm{V_{RMS}}$). However, the volt–ampere (V–A) characteristic exhibits a slight nonlinearity at higher voltages.
- The maximum peak-to-peak secondary voltage, $V_{\mathrm{PP}} = 20.6$ kV, was measured under open-circuit conditions (infinite secondary impedance). This corresponds to an effective turns ratio of
$$\frac{N_{\mathrm{sec}}}{N_{\mathrm{prim}}} = 34.$$
- The maximum primary current, $I_{\mathrm{prim,MAX}} = 32$ A, was observed when the secondary winding was short-circuited (zero impedance). This implies an estimated secondary short-circuit current of approximately
$$I_{\mathrm{sec,MAX}} \approx 1 \text{ A}.$$
- Under maximum load conditions, the effective primary input impedance was determined as
$$Z_{\mathrm{prim}} = \frac{\mathrm{d}U}{\mathrm{d}I} = 7.2\ \Omega,$$
corresponding to the configuration with the secondary winding fully loaded. This value is obtained as the inverse of the slope parameter from a first-order polynomial fit (pol1), yielding $p[1] = 0.139 \pm 0.003$.
- The maximum apparent power of the transformer was estimated as
$$P_{\max} = V_{\max} \cdot I_{\max} = 7.4 \text{ kVA}.$$
- The magnetic coupling factor K according to Eq. (1)
$$K = 0.98 \qquad \text{with } L_{+-} = 451/219 \text{ mH and } L_{P,S} = 10.7/325.8 \text{ mH}$$

The primary winding voltage regulated by an autotransformer.

2.2 Spark Gap Unit

The spark gap unit consists of four spark gap pairs connected in series. Each gap is formed by a pair of tungsten rods with a diameter of 10 mm and a length of 100 mm, with an adjustable inter-electrode distance. The rods are mounted in stainless steel bolts and equipped with eight cooling washers.

Fig. 3(a) shows the spark gap equipped with ventilators that inhibit the transition from transient streamer discharges to a stable arc by continuously flushing ionized air from the inter-electrode region. The outlet pipe for the extraction of ozone and other reactive species generated by the discharges is also visible. The two white cylinders on the left side of the figure correspond to two of the four primary resonant capacitors.

Fig. 3(b) spark gap unit with the outlet pipe and primary resonant capacitors removed.

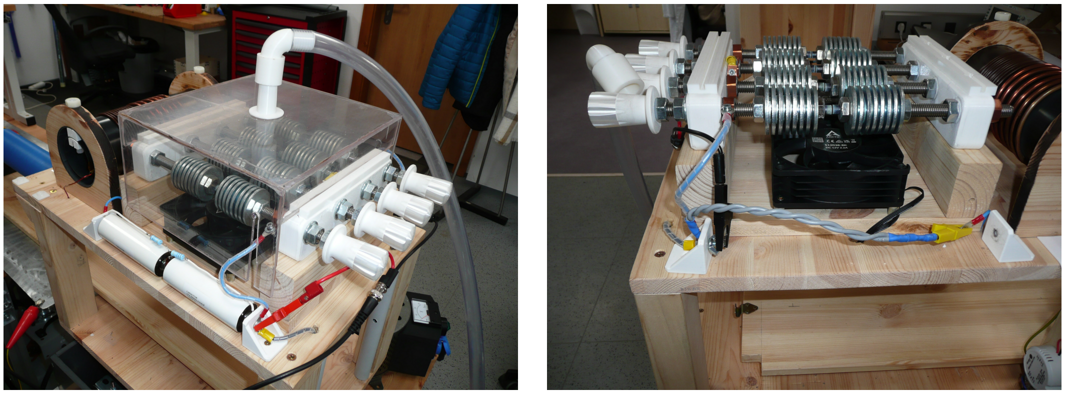

(a)

(b)

Figure 3: The spark gap unit consists of four spark gap pairs connected in series. Each gap is formed by a pair of tungsten rods with a diameter of 10 mm and a length of 100 mm, with an adjustable inter-electrode distance. The rods are mounted in stainless steel bolts and equipped with eight cooling washers.

2.3 Tesla Transformer used in DU

The Tesla Transformer (TT) employed in the Diathermy Unit (DU) consists of a concentric primary–secondary coil arrangement typical of spark-gap–driven Tesla systems. Both windings are supported on PVC cylindrical formers. The primary coil is wound on a PVC former with an outer diameter of 90 mm, while the secondary coil is wound on a PVC former with an outer diameter of 63 mm. The secondary coil is positioned coaxially inside the primary coil, as shown in Fig. 4(a).

The primary coil comprises six turns fabricated from copper tubing with an outer diameter of 4.76 mm. A selectable primary tap, labeled *Low*, is located at the fourth turn, allowing adjustment of the effective primary turn count and, consequently, the primary inductance and coupling to the secondary. A detailed view of the primary coil connections and tap arrangement is shown in Fig. 4(b).

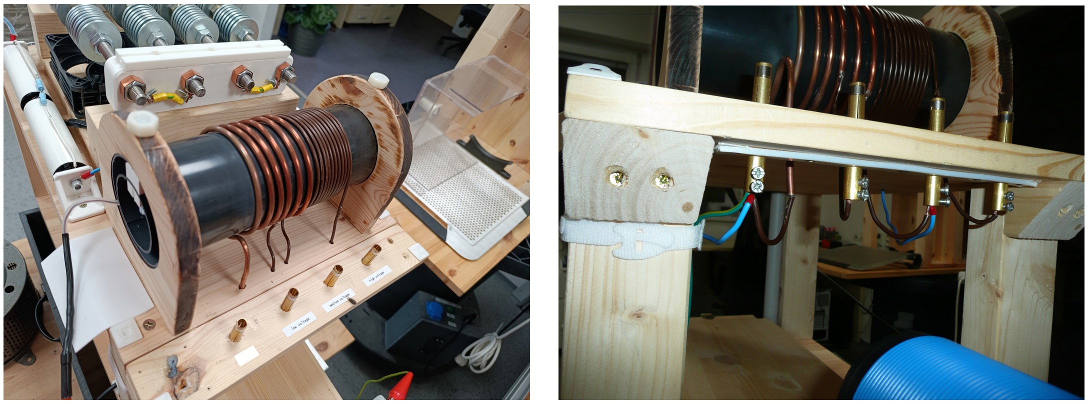

(a) (b)

Figure 4: (a) Tesla transformer overall view. (b) Detail view of TT connection.

Table 1: Measured and calculated inductances of the Tesla transformer coils. Inductances were measured at a frequency of 10 kHz.

Coil / Configuration	**Inductance** [μH]	**Turns** (N)	**Former diameter**
Primary coil (L_{prim})	2.9	6	$\phi = 90$ mm
Secondary coil (L_{sec})	227.6	98	$\phi = 63$ mm
Tertiary coil (L_{ter})	386.0	166	—
Primary + Secondary (aiding, L_+)	258.8	—	—
Primary + Secondary (opposing, L_-)	203.2	—	—

The magnetic coupling coefficient K between the primary and secondary windings of the Tesla transformer was determined using the series aiding/opposing inductance method.

According to

$$K = \frac{L_+ - L_-}{4\sqrt{L_1 L_2}}, \tag{1}$$

where $L_+ = L_{(\text{prim+sec}),+}$ and $L_- = L_{(\text{prim+sec}),-}$ denote the equivalent inductances of the primary and secondary coils connected in series in the aiding-field and opposing-field configurations, respectively. Using the measured values of L_+ and L_-, the coupling coefficient was found to be

$$\boxed{K = 0.54} \qquad M = K \cdot \sqrt{L_1 L_2} = 25.6\ \mu\text{H} \tag{2}$$

This value of K indicates relatively strong magnetic coupling between the primary and secondary coils. For comparison, the Golden Dragon Tesla transformer exhibits a magnetic coupling coefficient of $K = 0.365$. The primary resonant frequency, calculated using L_{prim} from Table 1 and the primary capacitance $C_{\text{prim}} = 8.75$ nF (see Fig. 2), is given by

$$f_{\text{prim}} = \frac{1}{2\pi\sqrt{L_{\text{prim}} C_{\text{prim}}}} \simeq 1\ \text{MHz}. \tag{3}$$

Consequently, for the measured value of t K given by Eq. (2), the expected mode splitting in the symmetric ($L_1 = L_2$ and $C_1 = C_2$) coupled-resonator spectrum is comparatively large. The normal-mode frequencies are

$$f_+ = \sqrt{1+K}\, f_{\text{prim}} \simeq 1.24\ \text{MHz},$$
$$f_- = \sqrt{1-K}\, f_{\text{prim}} \simeq 0.68\ \text{MHz}.$$

The above expressions apply to the symmetrical case and perfectly tuned to the same uncoupled resonant frequency. In the present DU system, this condition is not satisfied, and **the resonances are detuned**.

This behavior can be inferred from Fig. 5, where the frequency response of the DU system was characterized using a vector network analyzer (DG8SAQ VNWA). In Fig. 5(a), the blue solid line represents the primary LC resonator described by Eq. (3). The measured fundamental series resonance frequency is

$$f_{\text{prim,S}} = 0.81\ \text{MHz},$$

which is noticeably lower than the expected value of approximately 1 MHz given by Eq. (3). This downward shift is most likely attributable to the presence of parasitic capacitances in the circuit, loading effects introduced by the measurement setup, and possible frequency-dependent variations of the effective inductance.

The response of the secondary coil, measured in isolation from the primary, is shown as the blue line (*secondary solo*) in Fig. 5(b). Two characteristic resonances can be identified: the fundamental series resonance $f_{\text{sec,S}}$ and the parallel mode $f_{\text{sec,P}}$

$$f_{\text{sec,S}} = 2.81\ \text{MHz}, \tag{4}$$
$$f_{\text{sec,P}} = 3.96\ \text{MHz}/Z_{\text{sec,P}} = 151\text{k}\Omega. \tag{5}$$

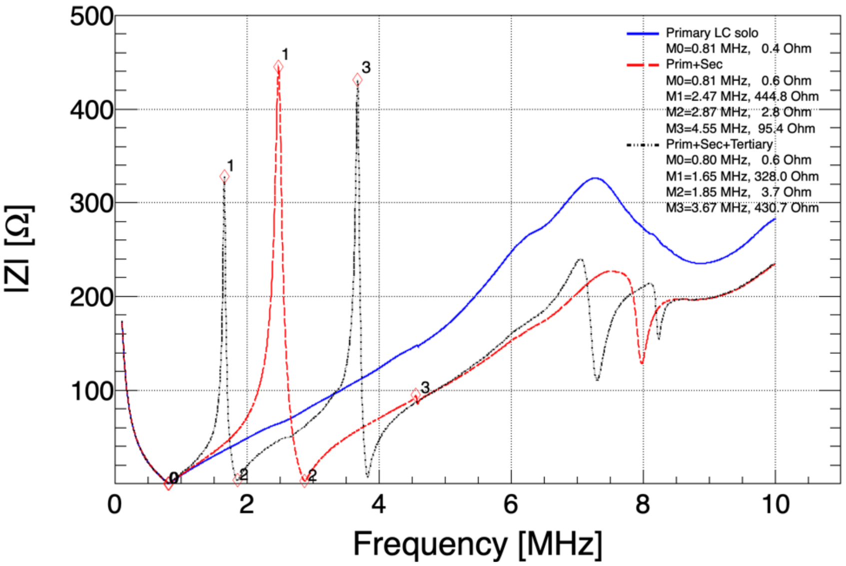

(a)

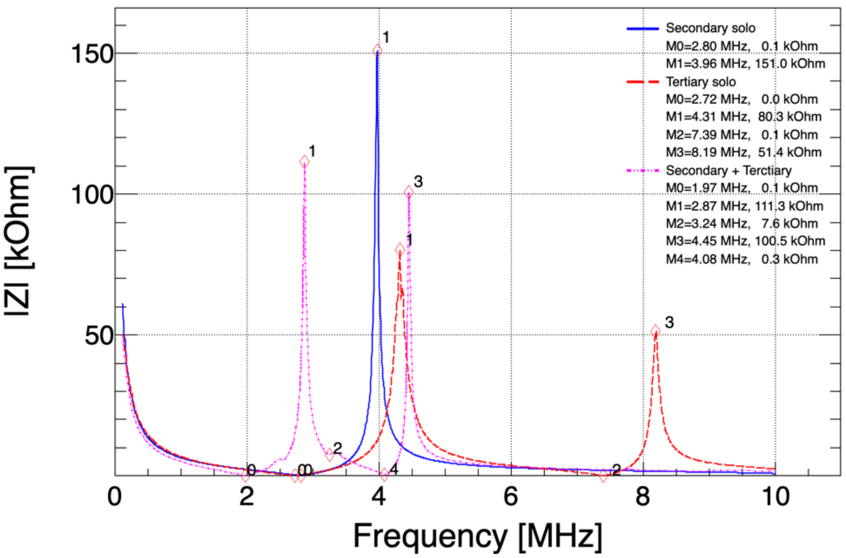

(b)

Figure 5: Measured frequency response of the resonant circuit integrated in DU, obtained using the DG8SAQ VNA. The meanings of the individual curves are explained in the legend.

The maximum energy and voltage transfer to the secondary coil occurs via the parallel mode of the secondary, since the secondary impedance is high in this regime and the voltage scales as

$$V_{\mathrm{sec}} \propto I_{\mathrm{sec}} \cdot Z_{\mathrm{sec,P}}.$$

However, in the present configuration the system operates in a detuned regime, such that this optimal condition for energy transfer is not fully achieved. As a consequence, the spectral content of the primary excitation overlaps only weakly with the high-Q parallel resonance of the secondary (for details see appendix A), limiting both the buildup of stored energy and the attainable secondary voltage.

2.4 Coupling of Strongly Detuned Resonators

The coupled system under investigation consists of two magnetically coupled resonators with substantially different natural frequencies: a primary LC resonator exhibiting a single series resonance at approximately $f_{\mathrm{prim}} \simeq 1$ MHz, and a secondary coil characterized by a series resonance at $f_{\mathrm{sec,S}} \simeq 2.8$ MHz and a parallel (anti-resonant) mode at $f_{\mathrm{sec,P}} \simeq 4.0$ MHz. Because the uncoupled resonance frequencies **differ by nearly a factor of three**, the system operates in a strongly detuned regime.

Hybridization of Resonance Modes

In coupled-resonator systems, *hybridization* refers to the formation of new normal modes (normal means orthonormal. For details see appendix B) that are linear combinations of the uncoupled resonator modes, leading to symmetric frequency splitting around a common resonance frequency. Such hybridization occurs only when the uncoupled resonance frequencies are comparable and the coupling strength is sufficiently large.

In the present case, the **large frequency detuning suppresses strong hybridization**. Instead of forming two symmetric split modes, each resonator largely preserves its original modal structure. The coupling manifests only as small frequency shifts and additional damping. Consequently, the classical normal-mode splitting relation

$$f_{\pm} = f_0\sqrt{1 \pm K}$$

is not applicable to the present system. This is demonstrated by the dashed red line in Fig. 5(a) and solid blue line in Fig. 5(a) which shows the frequency response of the uncoupled and coupled primary–secondary system.

$$\begin{aligned} f^{\mathrm{iso}}_{\mathrm{prim,S}} &= 0.81 \text{ MHz uncoupled } LC \\ f^{\mathrm{iso}}_{\mathrm{sec,S}} &= 2.81 \text{ MHz uncoupled} \\ f^{\mathrm{iso}}_{\mathrm{sec,P}} &= 3.96 \text{ MHz}/Z_{\mathrm{sec,P}} = 151\mathrm{k}\Omega \text{ uncoupled} \\ f^{\mathrm{cpl}}_{\mathrm{S}} &= 0.81 \text{ MHz coupled} \\ f^{\mathrm{cpl}}_{\mathrm{P}} &= 2.47 \text{ MHz}/Z_{\mathrm{sec,P}} = 445\Omega \text{ coupled} \end{aligned}$$

The first fundamental series resonance of the isolated primary LC circuit, $f^{\mathrm{iso}}_{\mathrm{prim,S}}$, coincides with the series-resonance frequency of the coupled primary–secondary system, $f^{\mathrm{cpl}}_{\mathrm{S}}$. In contrast, the uncoupled secondary parallel-resonance frequency, $f^{\mathrm{iso}}_{\mathrm{sec,P}}$, is shifted downward from 3.96 MHz to 2.47 MHz upon coupling, and the corresponding parallel impedance decreases by approximately a factor of 340. Since the parallel-resonance impedance scales linearly with the quality factor (see appendix A), the ratio of effective quality factors can be approximated as

$$\frac{Q_{\mathrm{iso}}}{Q_{\mathrm{cpl}}} \sim 340.$$

Taken together, the absence of observable mode splitting around $f^{\mathrm{iso}}_{\mathrm{prim,S}}$ and the strong suppression of the secondary parallel resonance indicate that, in this frequency range, the coupled system **does not exhibit appreciable mode hybridization.**

2.5 Damping of the Secondary Parallel Resonance

The pronounced damping of the secondary parallel (anti-resonant) mode observed in the coupled configuration is a direct consequence of additional loss channels introduced by magnetic coupling to the primary circuit. In the isolated configuration, the secondary parallel resonance represents a high-Q energy-storage mode, characterized by a large impedance peak. When coupled, this mode is transformed into a lossy system mode in which stored energy is rapidly extracted and dissipated.

At the secondary parallel resonance, inductive and capacitive reactances cancel, and the impedance is determined primarily by losses. In this regime, the parallel-resonance impedance scales approximately as

$$Z_{\mathrm{sec,P}} \approx Q_{\mathrm{sec}}\, \omega_0 L_{\mathrm{sec}}, \tag{6}$$

so that the impedance peak is directly proportional to the effective quality factor Q_{sec}.

When the primary and secondary coils are coupled, several additional loss mechanisms become active:

- **Magnetic back-coupling into the primary:** secondary currents induce currents in the primary, which dissipate energy in the primary resistance, spark gap, transformer losses, and wiring.
- **Detuning-induced decoherence:** because the primary and secondary resonances are strongly detuned, coherent cycle-by-cycle energy buildup in the secondary is suppressed.

As a result, the secondary parallel resonance ceases to function as a high-Q energy-storage mode and instead becomes an energy-transfer mode with rapid dissipation. This dramatic reduction of the effective Q explains the observed collapse of the impedance peak and the strong damping of the secondary parallel resonance. Under these conditions, voltage buildup on the secondary is severely limited, and efficient excitation of the Desmitron tube via the high-impedance secondary mode is not achieved. The VNWA data therefore provide direct experimental evidence that the present system operates in a strongly detuned and heavily loaded regime, rather than in a coherently coupled, high-Q resonant configuration.

2.5.1 Effective Inductive Loading and Secondary Modes

When the primary resonator operates near f_{prim}, the secondary coil is far from both its series and parallel resonances. Under these conditions, the secondary does not behave as a resonant system but instead presents an effective frequency-dependent *inductive load* to the primary. Physically, this corresponds to magnetically induced currents in the secondary that do not build up significant stored energy but nevertheless oppose the primary flux (Lenz's law), resulting in a downward shift of the primary resonance frequency and a reduction of its quality factor.

Conversely, near the secondary resonances ($f_{\mathrm{sec,S}}$ and $f_{\mathrm{sec,P}}$), the primary circuit is strongly detuned and behaves primarily as a lossy inductive element. Among the secondary modes, the parallel resonance plays a dominant role: at this frequency the secondary impedance is maximal, voltage amplitudes are strongly enhanced, and electromagnetic energy is preferentially stored in the distributed capacitance and magnetic field of the secondary coil.

2.5.2 Implications for Tesla Transformer Operation

As a result, the Tesla transformer does not operate through coherent oscillatory energy exchange between two matched resonators. Instead, the primary circuit acts as a broadband, impulsive energy source, injecting energy that is selectively captured and stored by the high-Q parallel resonance mode of the secondary. This mechanism explains **why efficient voltage buildup in the secondary can occur** even in the presence of strong frequency detuning and why precise primary–secondary frequency matching is not a strict requirement for operation.

In summary, the dominant energy transfer pathway in the present system is from the primary series resonance to the secondary parallel resonance, with the latter governing the overall electromagnetic response and voltage amplification of the Tesla transformer.

2.5.3 Minimal Impedance-Matrix Model for Two Magnetically Coupled Resonators

A compact way to formalize the above discussion is to model the primary and secondary circuits as two magnetically coupled current loops with mutual inductance $M = K\sqrt{L_1 L_2}$. In this minimal model, the coupling is purely magnetic and is treated as a perturbative loading of the individual resonators rather than as a fully symmetric coupling between two degenerate modes as described in the coupled-resonator eigenmode analysis presented in Appendix B. In particular, the primary series resonance remains essentially unchanged, while the secondary parallel resonance is strongly shifted and damped. As a result, no resonance splitting or formation of symmetric and antisymmetric hybrid modes is observed. The coupling therefore manifests as impedance modification and damping of the secondary response, rather than as true mode hybridization.

In the frequency domain (with the $e^{j\omega t}$ convention), the loop voltages and currents satisfy

$$\begin{bmatrix} V_1 \\ V_2 \end{bmatrix} = \begin{bmatrix} Z_1(\omega) & j\omega M \\ j\omega M & Z_2(\omega) \end{bmatrix} \begin{bmatrix} I_1 \\ I_2 \end{bmatrix},$$

where $Z_1(\omega)$ and $Z_2(\omega)$ are the uncoupled loop impedances. A minimal lumped representation consistent with a primary series tank and a secondary coil with distributed capacitance is

$$Z_1(\omega) = R_1 + j\omega L_1 + \frac{1}{j\omega C_1},$$
$$Z_2(\omega) = R_2 + j\omega L_2 + \frac{1}{j\omega C_2}.$$

Here, R_1 and R_2 represent effective loss terms (ohmic, dielectric, and radiative), and C_2 is an effective capacitance capturing the dominant self-capacitance (or top-load capacitance) of the secondary mode of interest. This model produces **one series resonance** for each loop and, in the coupled case, yields two system poles corresponding to the normal modes.

For the experimentally relevant case of a driven primary and an undriven secondary (i.e. $V_1 \neq 0$ and $V_2 = 0$), the secondary current can be eliminated:

$$I_2(\omega) = -\frac{j\omega M}{Z_2(\omega)}\, I_1(\omega). \tag{7}$$

Substitution into the primary equation yields an effective input impedance

$$Z_{\text{in}}(\omega) = \frac{V_1}{I_1} = Z_1(\omega) + \frac{\omega^2 M^2}{Z_2(\omega)}.$$

his expression makes the detuned-coupling behavior transparent. When the system is driven at the primary resonance frequency ω_1, which is well separated from the secondary resonance, the magnitude of the secondary impedance $|Z_2(\omega_1)|$ is large. Consequently, the coupling-induced correction term $\omega_1^2 M^2/Z_2(\omega_1)$ remains small, and the influence of the secondary on the primary resonance is negligible. The primary response is therefore only weakly perturbed, and the secondary appears mainly as a reactive load, which is predominantly inductive in the regime $\omega_1 \ll \omega_2$.

In contrast, near a secondary resonance the magnitude $|Z_2(\omega_2)|$ becomes small, and the coupling term increases accordingly. This leads to stronger loading of the primary and enhanced energy transfer into the secondary mode. The effective damping introduced into the primary response is governed by the real part $\mathrm{Re}\{Z_2(\omega_2)\} = R_2$ through the term $\omega^2 M^2/Z_2(\omega)$, thereby directly linking the quality factor of the secondary resonance to the observed behavior of the primary circuit.

Although energy transfer from the primary to the secondary can be strong when the system is driven at the secondary resonance frequency ω_2, this interaction manifests as dissipative loading rather than mode hybridization. In this regime, the primary circuit remains far from resonance and therefore does not respond resonantly. Instead, the primary acts as a source impedance that supplies energy to the secondary, rather than as a dynamically comparable partner oscillator capable of forming collective eigenmodes.

2.5.4 Connection to the VNWA-Measured Frequency Response

Equation (7) provides a direct interpretation of the features observed in the VNWA-measured frequency response shown in Fig. 5. In the VNWA measurement, the analyzer excites the primary circuit with a small-signal sinusoidal voltage while monitoring the resulting impedance or reflection response. The secondary winding is not externally driven, corresponding to the condition $V_2 = 0$.

At frequencies near the primary series resonance ($f_{\mathrm{prim,S}} \simeq 0.81$ MHz), the secondary presents a relatively large impedance, $Z_2(f_{\mathrm{prim,S}}) \approx 8\ \Omega$, compared to the coupling term. According to the relation (7), this implies that the induced secondary current I_2 remains small. Consequently, the secondary acts mainly as a weak, predominantly inductive load ($f_{\mathrm{prim,S}} \ll f_{\mathrm{sec,S}}$).

This loading results in a modest downward shift of the secondary parallel-resonance frequency $f_{\mathrm{sec,P}}$ from 3.96 MHz to 3.47 MHz and a strong reduction of the corresponding parallel impedance $Z_{\mathrm{sec,P}}$ from 151 kΩ to 445 Ω. Importantly, this behavior occurs without the appearance of symmetric mode splitting, indicating that the interaction manifests as dissipative loading rather than true mode hybridization.

In contrast, near the secondary resonances identified in Fig. 5(b), namely $f_{\mathrm{sec,S}} \simeq 2.80$ MHz the magnitude of the secondary impedance $|Z_2(f_{\mathrm{sec,S}})|$ is strongly reduced. As a consequence, the induced secondary current $I_2(\omega)$ becomes large, leading to pronounced magnetic back-action on the primary circuit.

Since the primary remains far from resonance at these frequencies, this interaction does not result in the formation of hybridized modes. Instead, the secondary resonance acts as a frequency-dependent load on the primary, introducing additional damping and reactive effects. In the VNWA response, this manifests as anti-resonant features, distortions, or increased loss rather than as symmetric frequency splitting around the primary resonance.

2.6 Primary characteristic impedance

$$Z_0 = \sqrt{\frac{L_{\text{prim}}}{C_{\text{prim}}}} = \sqrt{\frac{2.9 \cdot 10^{-6}}{8.75 \cdot 10^{-9}}} \simeq 18.2\ \Omega$$

For the same initial voltage, peak current scales roughly as:

$$I_{\text{pk}} \sim \frac{U}{Z_0}.$$

Using the $U_{\text{pk}} \approx 10$ kV we get the value of the peak current in the primary

$$I_{\text{pk}} \sim 550\ \text{A}$$

3 Tertiary Coil

This section analyzes why an additional galvanically connected but intentionally non-magnetically coupled “extra” (tertiary) coil can strongly reduce the observed parallel (anti-resonant) impedance of the coupled primary–secondary system, and provides a practical, VNA-driven mitigation strategy consistent with Tesla’s magnifying-transmitter logic.

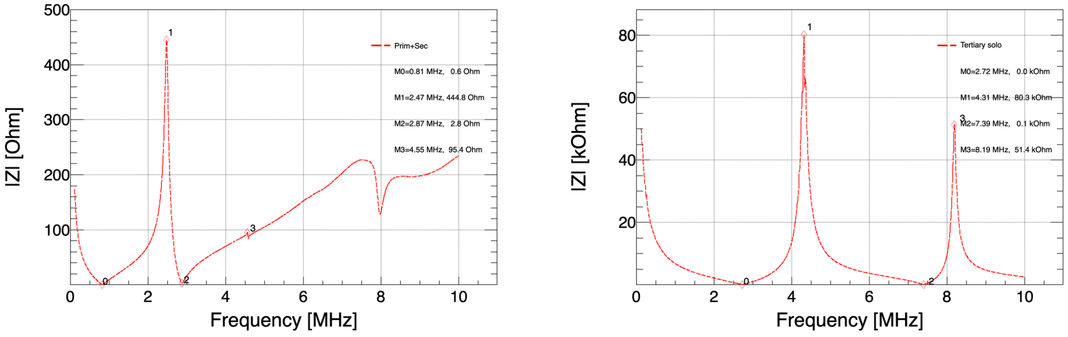

(a) (b)

Figure 6: (a) Frequency response of the primary LC circuit coupled to the secondary. (b) Frequency response of the tertiary coil with 166 turns and inductance $L_{\text{ter}} = 386\ \mu\text{H}$ (see Table 1).

Coupled primary+secondary . The measured input impedance magnitude $|Z|$ of the coupled primary–secondary system is shown in Fig. 6(a). The response exhibits a pronounced parallel resonance as well as at least one additional feature at higher frequencies. The marked points correspond to:

- M0: $f = 0.81$ MHz, $|Z| = 0.6\ \Omega$ (low-impedance region / series-like feature),
- M1: $f_p = 2.47$ MHz, $|Z| = 444.8\ \Omega$ (dominant parallel resonance peak),
- M2: $f = 2.87$ MHz, $|Z| = 2.8\ \Omega$ (series-like minimum following the peak),

The most important quantity for “voltage magnification” in the secondary is the dominant parallel peak at M1.

Tertiary coil solo. The tertiary coil measured standalone (Fig. 6(b).) shows a clear sequence of series and parallel resonances characteristic of a distributed helical resonator (slow-wave transmission line). The marked points are:

- M0: $f_{3,s1} = 2.72$ MHz, $|Z| \approx 0$ kΩ (series resonance / current maximum at the feed),

- M1: $f_{3,p1} = 4.31$ MHz, $|Z| \approx 80.3$ kΩ (parallel resonance / voltage maximum at the open end),
- M2: $f_{3,s2} = 7.39$ MHz, $|Z| \approx 0.1$ kΩ (next series resonance),
- M3: $f_{3,p2} = 8.19$ MHz, $|Z| \approx 51.4$ kΩ (next parallel resonance).

The fundamental parallel resonance is therefore

$$f_{3,p1} \approx 4.31 \text{ MHz}, \qquad |Z(f_{3,p1})| \approx 80.3 \text{ k}\Omega, \tag{8}$$

indicating that *the standalone tertiary coil itself is high-Q and not intrinsically lossy.*

3.1 Problem statement: why the parallel peak collapses when the tertiary is attached

The dominant coupled-system operating point is the strong parallel resonance at $f_p \approx 2.47$ MHz. A Tesla-correct extra coil must *not* demand significant RF current at this frequency, because the top of the secondary is near a voltage antinode and the resonator cannot supply large current without reducing its effective Q.

However, when the tertiary coil is galvanically connected to the secondary top node, the tertiary coil no longer behaves like the “solo” structure. Its modal frequencies shift because its effective capacitance increases due to:

1. **Added capacitive environment:** capacitance to the secondary body, to the top-load, and to surrounding grounded structures (walls, frames, instrumentation, floor).
2. **Junction-node stray capacitance:** the connection point (secondary top ↔ tertiary base) typically sees increased capacitance to ground, C_{jg}, which directly increases displacement current at a high-voltage node.
3. **Terminal (top-load) interaction:** the tertiary’s open-end capacitance (intentional terminal C_t plus stray) changes, shifting its parallel resonance downward.

Key mechanism. The tertiary coil acts as a *frequency-dependent impedance transformer* connected at the highest-voltage point of the secondary. If, at or near f_p, the tertiary presents a relatively *low* impedance (or a lossy impedance) at its base, it behaves as a **shunt load at a voltage antinode**, forcing current and collapsing the system’s parallel peak impedance.

Why the measured frequencies are "dangerous". The standalone tertiary has $f_{3,p1} = 4.31$ MHz and $f_{3,s1} = 2.72$ MHz. The coupled system's main peak is $f_p = 2.47$ MHz, which lies only about 9% below the tertiary's first *series* resonance:

$$\frac{f_p}{f_{3,s1}} \approx \frac{2.47}{2.72} \approx 0.91. \tag{9}$$

This is critical: *operating near the tertiary's series resonance is the worst possible regime*, because the tertiary base impedance becomes small and current demand becomes large. When connected, the tertiary's resonances typically shift downward (due to increased capacitance), pushing $f_{3,s1}$ even closer to (or below) f_p, making the loading stronger.

Practical symptom (what VNWA shows). This mechanism manifests as:

- strong reduction of the coupled-system $|Z|$ peak near f_p (effective Q collapse),
- broadening of the resonance (increased damping),
- appearance of new notches/shoulders near the operating band due to tertiary mode interaction.

Importantly, this is *not* primarily ohmic loss in the tertiary (the solo peak is ~ 80 kΩ), but rather *reactive loading and displacement-current loss* induced by the connection geometry and the shifted modal alignment.

3.2 Equivalent-circuit interpretation (lumped + distributed)

A useful minimal equivalent circuit at the secondary top node is:

- coupled primary–secondary system represented by an effective parallel resonance at f_p with finite loss (effective $R_{\|}$),
- tertiary coil represented by an input impedance $Z_{in,3}(\omega)$ connected from the top node to its open end terminal capacitance C_t,
- stray capacitance at the junction node to ground C_{jg}.

In distributed form, the tertiary is a helical transmission-line section with characteristic impedance $Z_{0,3}$ and electrical length $\theta_3 = \beta_3 \ell_3$, terminated by $Z_L = 1/(j\omega C_t)$. The input impedance seen at the base is

$$Z_{in,3}(\omega) = Z_{0,3}\,\frac{Z_L + jZ_{0,3}\tan\theta_3}{Z_{0,3} + jZ_L\tan\theta_3}. \tag{10}$$

The coupled system "survives" (high $|Z|$ at f_p) only if, at $\omega_p = 2\pi f_p$,

$$|Z_{in,3}(\omega_p)| \gg |Z_{\text{top}}(\omega_p)|, \qquad \text{and ideally} \qquad \text{Im}\{Z_{in,3}(\omega_p)\} > 0, \tag{11}$$

i.e. the tertiary appears as a **high, mostly inductive impedance** at the operating frequency, drawing minimal current.

The present standalone measurements indicate the opposite risk: since f_p lies close to the tertiary series resonance $f_{3,s1}$, $Z_{in,3}(\omega_p)$ can become small when the coil is attached and detuned downward, violating (11).

3.3 Design objectives (Tesla-correct extra coil)

A Tesla-correct extra coil must satisfy these objectives when attached to the secondary:

1. **Avoid series-resonant alignment near f_p:** ensure the tertiary's *first series* resonance remains well above f_p even after attachment.
2. **Keep the tertiary base impedance high at f_p:** enforce (11) by geometry and terminal tuning.
3. **Minimize junction-node stray capacitance C_{jg}:** reduce displacement current from the top node to ground.
4. **Tune with a smooth terminal, not with extra turns:** prefer controlled terminal capacitance C_t rather than increasing turns/length, which increases stray coupling and lowers modal frequencies unpredictably.

3.4 Concrete problems identified from the two plots

From `ModZP+S.png` and `TercSolo.png`, the primary issues are:

P1: The system operating frequency is too close to the tertiary's first series resonance. With $f_p = 2.47$ MHz and $f_{3,s1} = 2.72$ MHz (solo), the margin is small and becomes worse after attachment. This makes the tertiary behave like a current-hungry branch at f_p.

P2: Attachment will shift tertiary resonances downward (increased effective capacitance). Therefore, the "solo" tertiary response is optimistic; once connected, $f_{3,s1}$ and $f_{3,p1}$ shift toward the operating band, increasing loading.

P3: Junction-node stray capacitance C_{jg} can dominate. Even if the tertiary modes are moved away, a large C_{jg} (due to physical layout, proximity to ground, scope leads, metal supports) creates large displacement current at the top node and reduces the measured $|Z|$ peak.

3.5 Mitigation strategy (VNA-driven, step-by-step)

The following procedure is intended to be deterministic: each change is validated by observing whether the coupled-system peak at f_p recovers in magnitude and sharpness.

3.5.1 Step 1: Push the tertiary *series* resonance away from f_p

The dominant risk is $f_{3,s1}$ approaching f_p. Therefore:

- **Shorten the tertiary (remove turns / reduce height)** to raise both $f_{3,s1}$ and $f_{3,p1}$.
- **Prefer a larger diameter with fewer turns** rather than a long, thin coil. This tends to raise self-resonance and reduce sensitivity to the environment.

Target (practical rule):

$$f_{3,s1,\text{attached}} \gtrsim 1.3\, f_p, \qquad \Rightarrow \qquad f_{3,s1,\text{attached}} \gtrsim 3.2 \text{ MHz}. \tag{12}$$

Because attachment shifts frequencies downward, the *solo* tertiary should be higher than this target.

3.5.2 Step 2: Keep the tertiary *parallel* resonance safely above the operating band

Operate the extra coil below its own parallel resonance so that it appears inductive at the base (low current draw). A practical Tesla window is:

$$f_{3,p1,\text{attached}} \approx (1.2\text{–}1.35)\, f_p \qquad \Rightarrow \qquad f_{3,p1,\text{attached}} \approx 3.0\text{–}3.3 \text{ MHz}. \tag{13}$$

Since attachment shifts $f_{3,p1}$ downward, the *solo* tertiary should be designed with $f_{3,p1,\text{solo}}$ noticeably above the desired attached value, then pulled down by controlled terminal capacitance (next step).

3.5.3 Step 3: Tune with terminal capacitance, not with turns

Once the tertiary geometry is shortened such that its modes are comfortably above f_p, add a *smooth* terminal (small toroid or sphere) to set $f_{3,p1,\text{attached}}$ within the Tesla window (13).

- Increasing C_t lowers $f_{3,p1}$ in a controlled, low-loss manner.
- Adding turns lowers $f_{3,p1}$ but also increases stray coupling, increases C_{jg}, and increases the risk of bringing $f_{3,s1}$ into the operating band.

3.5.4 Step 4: Minimize C_{jg} by physical placement and routing

Even a well-tuned extra coil will fail if C_{jg} is large. Apply:

- Place the tertiary **inside the top-load field zone** (near the toroid/sphere), not hanging downward.
- Maximize clearance to ground and nearby metal (including measurement fixtures and instrument cables).
- Use short, direct, low-profile connection at the junction; avoid large exposed junction conductors.
- Avoid dielectrics with loss tangent near strong E-fields (supports close to the top node).

3.5.5 Step 5: VNWA validation criteria

After each modification, re-measure the coupled primary+secondary with the tertiary attached and evaluate:

1. Does the dominant peak near $f_p \approx 2.47$ MHz retain a high magnitude (comparable to the baseline 444.8 Ω)?
2. Does the peak remain sharp (not strongly broadened)?
3. Are new notches or shoulders introduced close to f_p (indicating residual series/parallel interaction)?

Success criterion (practical):

$$|Z'(f_p)| \gtrsim 0.7\,|Z(f_p)|, \tag{14}$$

with preference for $|Z'(f_p)| \approx |Z(f_p)|$ or higher.

3.6 Summary: what is wrong and what fixes it

The measurements show a coupled-system operating peak at $f_p = 2.47$ MHz and a standalone tertiary whose first series resonance is at 2.72 MHz. This proximity means that, upon attachment (which shifts tertiary resonances downward and increases stray capacitance at the junction), the tertiary presents a low or lossy impedance at the secondary top node, forcing current at a voltage antinode and collapsing the parallel impedance peak.

The Tesla-correct remedy is therefore:

1. **Raise the tertiary's series resonance away from f_p** by shortening the tertiary (remove turns / reduce height) and favoring larger diameter/fewer turns.

2. **Operate below the tertiary's parallel resonance** so the tertiary appears inductive at its base at f_p.
3. **Tune primarily with a smooth terminal capacitance** rather than geometry changes that increase stray coupling.
4. **Aggressively reduce junction-to-ground capacitance** C_{jg} by placement, clearance, and wiring/layout.

Following this procedure converts the tertiary from a peak-killing shunt branch into a true "extra coil" that can support voltage magnification without degrading the primary–secondary resonance.

4 Desmitron tubes Optical and thermal spectra

We received three desmitron tubes manufactured by Griffin, listed in Table 2. Tube #2 exhibits a markedly different emission color compared to Tube #1, and during testing with the Golden Dragon Tesla transformer the aluminum pad overheated and melted. Tube #3 appears mechanically intact; however, no photo-fluorescent response was observed in any of our tests. Tube #1 is fully operational, and all experimental results presented in this document were obtained using this tube.

Table 2: Status and optical response of three desmitron tubes.

Tube	Status / Observation
#1	Operational; weak spot intensity on fluorescent screen
#2	Non-operational; aluminum pad melted during operation
#3	Operational; no shadow observed on fluorescent screen

Optical emission spectra were measured for Tube #1 and Tube #3; the results are shown in Fig. 7.

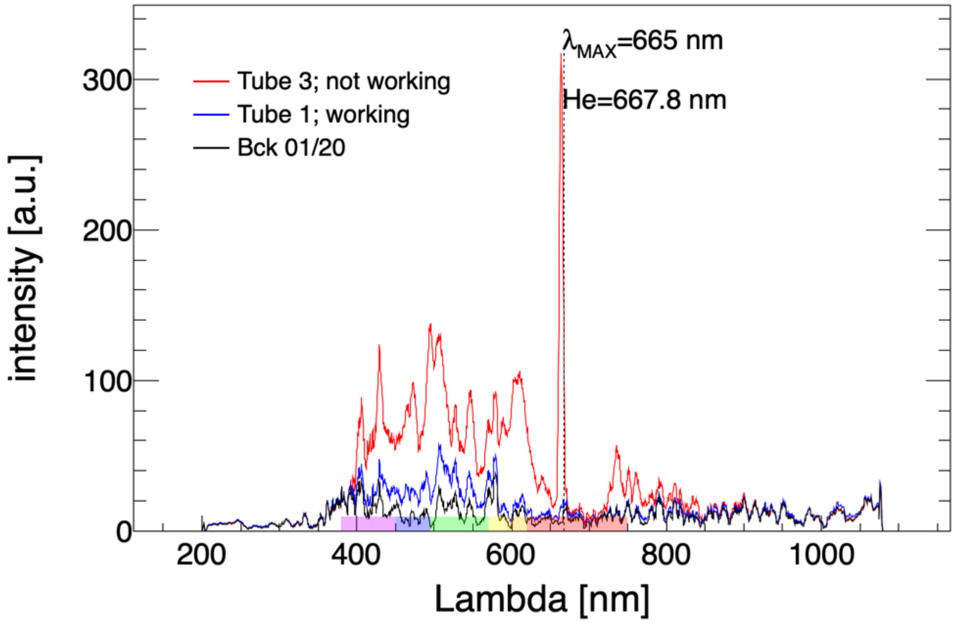

Figure 7: Measured optical emission spectra of Tube #1 (blue) and Tube #3 (red), with the background spectrum shown in black.

Tube #1 exhibits only a moderate increase in optical emission intensity in the wavelength range 400–600 nm. In contrast, Tube #3 shows a substantially stronger emission in this region and, in addition, a pronounced spectral peak at approximately 665 nm, which is absent in Tube #1. This wavelength is close to the helium emission line at $\lambda_{\mathrm{He}} = 667.8$ nm.

The presence of this line suggests residual gas emission, indicating imperfect vacuum conditions in Tube #3. We therefore attribute the absence of any observable photofluorescent response from Tube #3 to vacuum degradation, which likely alters the emission mechanism and suppresses the production of the radiation responsible for fluorescence excitation.

We observe that the background spectrum exhibits the same fine structure as shown in Fig. 8. Measurements were performed with the optical sensor fully shielded or electrically disconnected. As can be seen, the fine spectral features are reproduced almost identically in all runs, indicating that they are not of statistical origin. This suggests that the background distribution is deterministic and can, in principle, be subtracted from the measured signal.

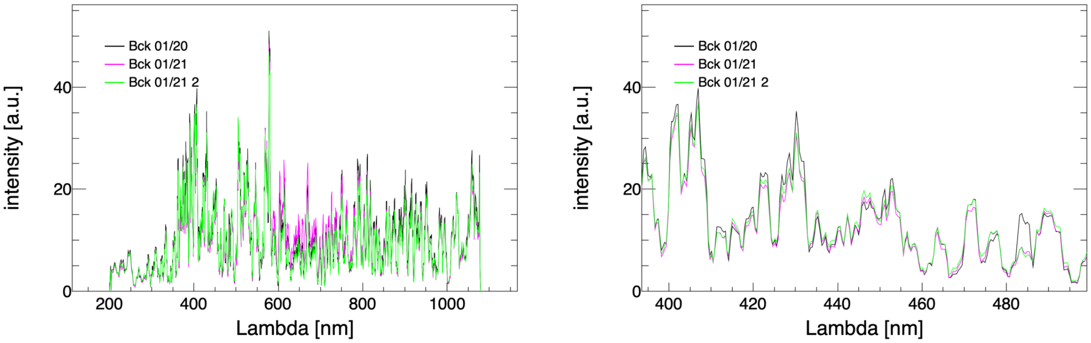

Figure 8: Background optical spectra measured in three independent runs with the optical sensor shielded and/or disconnected. The left panel shows the full wavelength range, while the right panel presents a zoomed-in section. The observed fluctuations do not appear to be of purely statistical origin.

Thermal images of Tube #1 acquired with a thermal camera after 20 s (Fig. 9(a)) and 40 s (Fig. 9(b)) of continuous operation reveal two prominent localized warm regions. These hot spots likely correspond to antinodes of standing electromagnetic waves within the tube. The first hot spot is located between the anode and the spherical end of the tube, while the second appears at the apex of the spherical section. After 40 s of operation, the maximum observed surface temperature reaches approximately 60 °C.

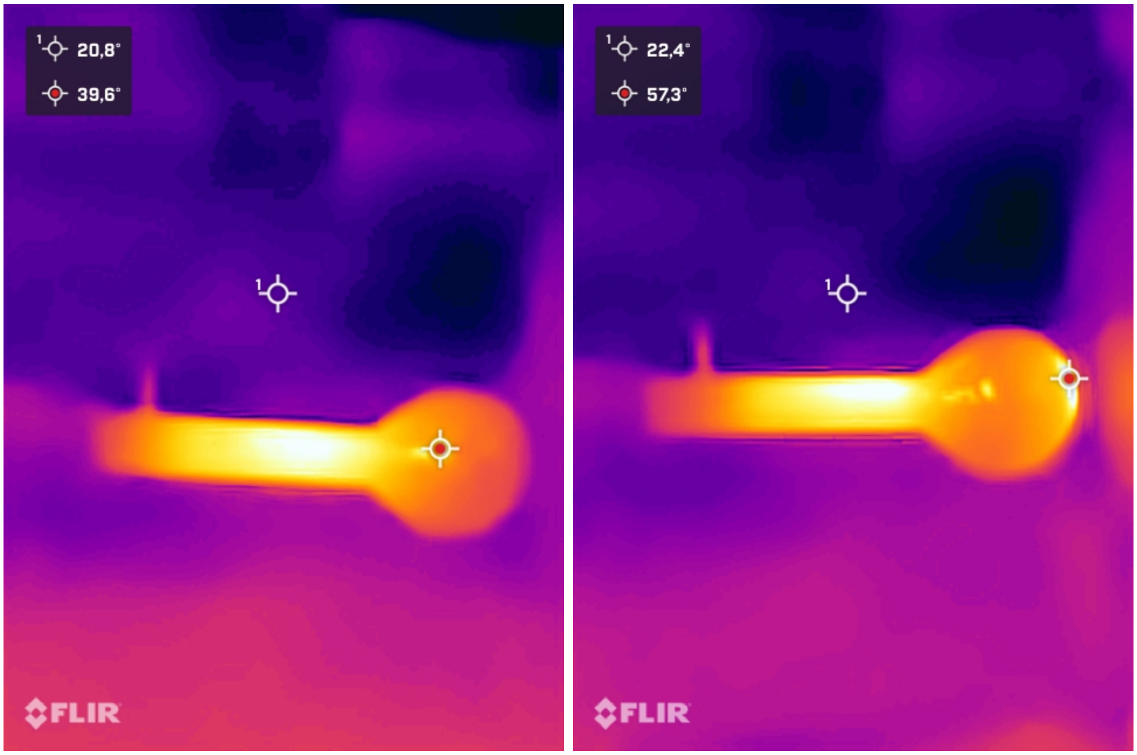

Figure 9: Thermal images of Tube #1 acquired with a thermal camera after 20 s (a) and 40 s (b) of continuous operation.

5 Shadowgraph results

The photo-fluorescent screen is enclosed in a wooden box containing a GoPro camera, as shown in Fig. 10(a). The box is illuminated externally by the desmitron tube. To visualize the resulting “shadow,” a small copper plate with a circular aperture was placed near the tube exit, between the tube and the box. The shadow recorded by the camera is shown in Fig. 10(b). The black rectangle corresponds to a piece of plastic tape placed inside the box for camera adjustment.

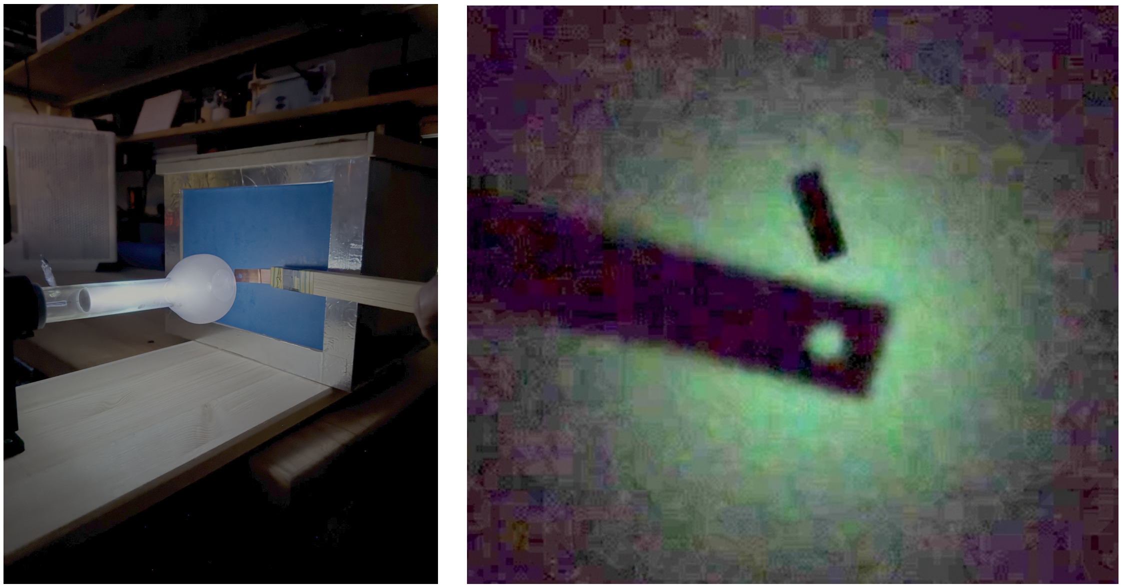

(a) (b)

Figure 10: Typical picture from the GoPro camera inside the closed box with photo-fluorescent screen

The shadow is clearly visible; however, compared to Griffin’s observations, its contrast is significantly weaker. We also observed that the fluorescent emission intensity decreases rapidly with distance from the tube. At distances greater than approximately 10 cm, the green fluorescence vanishes completely and no shadow can be detected. This work discusses the likely causes of this behavior, and an improved experimental setup is currently under construction.

A Meaning and Role of a High-Q Resonant System

Definition of the Quality Factor

The quality factor Q of a resonant system quantifies the efficiency with which the system stores energy relative to its losses. It is defined as

$$Q = 2\pi \frac{\text{energy stored in the resonator}}{\text{energy dissipated per cycle}}. \tag{15}$$

An equivalent frequency-domain definition is

$$Q = \frac{\omega_0}{\Delta\omega}, \tag{16}$$

where ω_0 is the angular resonance frequency and $\Delta\omega$ is the full width at half maximum (FWHM) of the resonance peak.

Physical Interpretation of High-Q

A resonant system with high Q exhibits the following characteristics:

- **Efficient energy storage:** most of the electromagnetic energy oscillates between electric and magnetic forms, with minimal dissipation per cycle.
- **Slow energy decay:** when excitation is removed, the stored energy decays exponentially,
$$W(t) \propto \exp\left(-\frac{\omega_0 t}{Q}\right).$$
- **Narrow bandwidth:** the resonance responds strongly only within a narrow frequency interval,
$$\Delta f = \frac{f_0}{Q}.$$
- **Large field amplitudes:** high voltages or currents can be sustained at resonance.

Series and Parallel Resonance

The meaning of high Q depends on the resonance type:

- **Series resonance** corresponds to a minimum impedance and maximized current. The quality factor is primarily limited by series losses.
- **Parallel (anti-)resonance** corresponds to a maximum impedance and maximized voltage. In this case, a high Q implies strong electric-field buildup and large voltage amplitudes.

In Tesla-transformer systems, the secondary parallel resonance typically exhibits the highest Q and therefore dominates voltage buildup.

High-Q and Energy Transfer in the Tesla Transformer

In a magnetically coupled system, efficient energy transfer requires that the excitation spectrum overlaps the resonance bandwidth. For a high-Q secondary mode, the effective impedance near parallel resonance scales approximately as

$$Z_{\mathrm{sec,P}} \sim Q\,\omega_0 L_{\mathrm{sec}}, \tag{17}$$

leading to a secondary voltage

$$V_{\mathrm{sec}} \propto Q \cdot I_{\mathrm{sec}}. \tag{18}$$

Thus, a high Q enables voltage accumulation over many cycles, provided that losses and detuning are sufficiently small.

Impact of Detuning and Loading

While a high-Q resonance allows large energy storage, it is also highly frequency-selective. Detuning between the excitation frequency and the resonance frequency significantly reduces energy transfer efficiency. Additionally, loading effects—such as resistive losses, radiation, plasma formation, or attachment of external devices—reduce the effective Q, broaden the resonance, and limit the attainable voltage and stored energy.

In summary, a high-Q resonant mode is essential for efficient energy accumulation and voltage amplification in Tesla-transformer systems, but its benefits are realized only when excitation, coupling, and loading conditions are appropriately matched.

B Two coupled LC resonators

We consider two lossless LC resonators with inductances L_1, L_2 and capacitances C_1, C_2, coupled via a mutual inductance M. Let $i_1(t)$ and $i_2(t)$ denote the loop currents of the two resonators. Applying Kirchhoff's voltage law yields

$$\begin{aligned} L_1\frac{di_1}{dt} + M\frac{di_2}{dt} + v_1 &= 0, \\ M\frac{di_1}{dt} + L_2\frac{di_2}{dt} + v_2 &= 0, \end{aligned}$$

with the capacitor relations

$$i_1 = C_1\frac{dv_1}{dt}, \qquad i_2 = C_2\frac{dv_2}{dt}.$$

Differentiating the loop equations and substituting the capacitor currents leads to the second-order system

$$\begin{aligned} L_1\ddot{i}_1 + M\ddot{i}_2 + \frac{1}{C_1}i_1 &= 0, \\ M\ddot{i}_1 + L_2\ddot{i}_2 + \frac{1}{C_2}i_2 &= 0. \end{aligned}$$

Assuming harmonic solutions of the form $i_k(t) = I_k e^{j\omega t}$ results in the algebraic eigenvalue problem

$$\begin{bmatrix} \frac{1}{C_1} - \omega^2 L_1 & -\omega^2 M \\ -\omega^2 M & \frac{1}{C_2} - \omega^2 L_2 \end{bmatrix} \begin{bmatrix} I_1 \\ I_2 \end{bmatrix} = \mathbf{0}.$$

B.1 Eigenfrequencies

Nontrivial solutions exist when the determinant of the system matrix vanishes,

$$\left(\frac{1}{C_1} - \omega^2 L_1\right)\left(\frac{1}{C_2} - \omega^2 L_2\right) - \omega^4 M^2 = 0.$$

This condition yields two eigenfrequencies $\omega_\pm$, corresponding to the two normal modes of the coupled system.

Introducing the uncoupled resonance frequencies

$$\omega_1 = \frac{1}{\sqrt{L_1 C_1}}, \qquad \omega_2 = \frac{1}{\sqrt{L_2 C_2}},$$

and the coupling coefficient

$$k = \frac{M}{\sqrt{L_1 L_2}},$$

the eigenfrequencies can be written as

$$\omega_\pm^2 = \frac{\omega_1^2 + \omega_2^2 \pm \sqrt{(\omega_1^2 - \omega_2^2)^2 + 4k^2\omega_1^2\omega_2^2}}{2(1-k^2)}. \tag{19}$$

B.2 Eigenvectors and amplitude ratios

For each eigenfrequency $\omega_\pm$, the corresponding eigenvector $(I_1, I_2)^\mathsf{T}$ follows directly from the linear system. From the first row of the matrix equation one obtains

$$\frac{I_2}{I_1} = \frac{\frac{1}{C_1} - \omega_\pm^2 L_1}{\omega_\pm^2 M}.$$

An equivalent expression is obtained from the second row,

$$\frac{I_2}{I_1} = \frac{\omega_\pm^2 M}{\frac{1}{C_2} - \omega_\pm^2 L_2},$$

with both expressions being identical provided that the determinant condition is satisfied. The eigenvector associated with each normal mode may therefore be written as ($I_1 \equiv 1$)

$$\mathbf{v}_\pm \propto \begin{bmatrix} 1 \\ \dfrac{\frac{1}{C_1} - \omega_\pm^2 L_1}{\omega_\pm^2 M} \end{bmatrix}, \tag{20}$$

up to an arbitrary normalization factor.

B.3 Hybridization versus localization

The ratio I_2/I_1 provides direct physical insight into the nature of the normal modes.

Near degeneracy ($\omega_1 \approx \omega_2$ and this implies $|Z_1(\omega)| \approx |Z_2(\omega)|$). When the uncoupled resonators are nearly identical, coupling **hybridizes** their modes, resulting in two collective normal modes with eigenfrequencies $\omega_\pm$. In this regime, both eigenmodes exhibit $|I_2/I_1| \sim \mathcal{O}(1)$, indicating that the currents in the two resonators are of comparable magnitude. In the time domain, coupling generally leads to **beating**; however, this depends on the mode of excitation.

(A) If both resonators are excited directly in one of the normal modes—i.e. at $\omega_\pm$ with the corresponding current amplitude ratio I_2/I_1 and phase relation—only a single eigenmode is populated. In this case, the oscillation remains stationary and no beating occurs.

(B) If the excitation does not match a normal mode, for example when only the primary resonator is excited or when the excitation frequency differs from $\omega_\pm$, both normal modes are simultaneously populated. Their superposition results in beating, observed as a periodic exchange of energy between the resonators.

Strong detuning ($|\omega_1 - \omega_2|$ large). For sufficiently different uncoupled resonance frequencies, the amplitude ratio becomes strongly asymmetric. One eigenmode satisfies $|I_2/I_1| \ll 1$ and is predominantly localized in resonator 1, while the other mode satisfies $|I_2/I_1| \gg 1$ and is localized in resonator 2. In this limit, hybridization is weak and the coupling induces only small frequency shifts rather than pronounced mode splitting.

These two regimes—hybridization near degeneracy and localization under strong detuning—provide a unified framework for interpreting mode splitting and mode participation observed in frequency-domain measurements of coupled resonant systems.

B.4 In-phase and out-of-phase normal modes

For two coupled resonators, the normal modes can be classified according to the relative phase of the oscillations in the two resonators.

- In the *in-phase* (symmetric) mode, the currents in both resonators oscillate with the same phase, $I_2/I_1 > 0$. As a result, the electromagnetic fields generated by the two resonators reinforce each other, and the energy distribution remains symmetric. Depending on the sign and strength of the coupling, this mode corresponds to either the lower or higher eigenfrequency of the coupled system.
- In the *out-of-phase* (antisymmetric) mode, the currents oscillate with opposite phase, $I_2/I_1 < 0$. In this case, the fields partially cancel in the coupling region, leading to a different effective restoring force and hence a different eigenfrequency. This mode represents a distinct collective oscillation of the coupled system.

These two phase configurations constitute the eigenstates of the coupled system. When the system is excited exactly in one of these modes, the relative phase and amplitude relations remain fixed in time and no energy exchange between the resonators occurs. Any excitation that does not match one of these phase relations results in a superposition of the in-phase and out-of-phase modes, giving rise to beating in the time-domain response.

C Hybridized modes in a Tesla transformer: transference and displacement regimes

When a Tesla transformer is tuned close to degeneracy between the primary and secondary resonators, coupling leads to hybridization and the emergence of two collective normal modes with eigenfrequencies $\omega_\pm$. These modes are distinguished by the relative phase of the currents in the primary and secondary and correspond to qualitatively different electromagnetic field configurations.

C.1 In-phase and out-of-phase hybridized modes

In the lower-frequency hybridized mode, the primary and secondary currents oscillate *in phase*, i.e. $I_2/I_1 > 0$. In this configuration, the magnetic fields generated by the two resonators add constructively, resulting in an increased effective inductance of the coupled system and hence a reduced resonance frequency. Energy exchange is dominated by inductive coupling, and electromagnetic energy remains largely confined within the coupled resonator system.

In contrast, the higher-frequency hybridized mode corresponds to *out-of-phase* currents, $I_2/I_1 < 0$. Here, the magnetic fields partially cancel in the coupling region, leading to a reduced effective inductance and an increased eigenfrequency. The magnetic energy stored in the system is lower, while electric field gradients become more pronounced, particularly near the secondary terminal. It amplifies the **Near-field** phenomena and suppresses the magnetic field.

C.2 Transference and displacement in Maxwellian terms

These two hybridized modes can be rigorously interpreted within Maxwell's equations without invoking additional physical mechanisms. In the in-phase mode, energy transfer between the resonators is governed primarily by conduction currents and their associated magnetic fields. This regime corresponds to what may be termed a *transference mode*, in which power flow is mediated predominantly by inductive coupling and the Poynting vector remains largely confined to the near-field region of the coils.

In the out-of-phase mode, the reduced magnetic coupling leads to a relative enhancement of electric fields and displacement currents, as described by Maxwell's correction to Ampère's law. The electromagnetic energy density shifts toward electric-field dominance, and the spatial extent of the near field increases. This regime corresponds to what has historically been referred to as a *displacement-dominated* mode. Importantly, this description remains fully consistent with classical electrodynamics: no superluminal signal propagation or non-Hertzian radiation is implied, and all energy transport remains causal.

D Quarter-wave condition of the tertiary (transmission-line) resonator

Model the tertiary as a lossless helical transmission-line section with characteristic impedance $Z_{0,3}$ and electrical length $\theta_3 = \beta_3 \ell_3$, terminated at the top by the effective capacitance C_t, i.e.

$$Z_L(\omega) = \frac{1}{j\omega C_t} = -jX_c(\omega), \qquad X_c(\omega) = \frac{1}{\omega C_t}. \tag{21}$$

The input impedance at the base is (standard lossless transmission-line result)

$$Z_{in,3}(\omega) = Z_{0,3}\,\frac{Z_L + jZ_{0,3}\tan\theta_3}{Z_{0,3} + jZ_L\tan\theta_3}. \tag{22}$$

Substituting $Z_L = -jX_c$ gives

$$Z_{in,3}(\omega) = jZ_{0,3}\,\frac{Z_{0,3}\tan\theta_3 - X_c}{Z_{0,3} + X_c\tan\theta_3}, \tag{23}$$

which is purely reactive in the lossless limit.

High-impedance (quarter-wave) condition. For Tesla-style operation, the desired regime is a large input impedance at the base (minimal base current and strong voltage magnification). This occurs when the denominator of (23) approaches zero,

$$Z_{0,3} + X_c(\omega)\tan\theta_3(\omega) \approx 0 \quad \Rightarrow \quad \tan\theta_3(\omega) \approx -\omega C_t Z_{0,3}. \tag{24}$$

Equation (24) is the exact “quarter-wave” condition for a capacitive termination. In the common case where the top capacitance is sufficiently large such that $\omega C_t Z_{0,3} \gg 1$, the solution requires $|\tan\theta_3| \gg 1$, and therefore

$$\theta_3(\omega) \approx \frac{\pi}{2} + n\pi \; + \; \delta, \qquad \delta \approx \frac{1}{\omega C_t Z_{0,3}}, \qquad n \in \mathbb{Z}, \tag{25}$$

i.e. the resonance is close to an odd quarter-wave, slightly shifted by the finite capacitive load.

Low-impedance condition (for completeness). A minimum of the input impedance occurs when the numerator of (23) vanishes,

$$Z_{0,3} \tan\theta_3(\omega) - X_c(\omega) \approx 0 \quad \Rightarrow \quad \tan\theta_3(\omega) \approx \frac{1}{\omega C_t Z_{0,3}}, \tag{26}$$

which approaches $\theta_3 \simeq n\pi$ for $\omega C_t Z_{0,3} \gg 1$.

Design implication. Given a target operating frequency ω_p, the tertiary length (or effective capacitance) can be chosen such that (24) holds at ω_p, ensuring that $|Z_{in,3}(\omega_p)|$ is large. Furthermore, choosing the operating point slightly below the quarter-wave condition makes $Z_{in,3}(\omega_p)$ predominantly inductive, which helps to minimize current draw from the coupled primary–secondary system and preserves a high $|Z|$ at the operating resonance.

References

[1] `https://am-innovations.com/hg-fischer-diathermy/`

[2] `https://am-innovations.com/spark-gap-generator-part-1/`